Ahmad, N., Núñez-Sánchez, S., Pugh, J. R., & Cryan, M. J. (2016). Deep-groove nickel gratings for solar thermal absorbers. *Journal of Optics*, *18*(10), [105901]. https://doi.org/10.1088/2040-8978/18/10/105901

Deep-Groove Nickel Gratings for Solar Thermal Absorbers

N.Ahmad, S.Núñez-Sánchez, J.R.Pugh and M.J.Cryan

Department of Electrical and Electronic Engineering, University of Bristol
E-mail: M.Cryan@bristol.ac.uk

ABSTRACT

This paper presents measured and modelled optical absorptance and reflectance for deep-groove nickel nano-gratings in the 450nm-950nm wavelength range. The structures have been fabricated using focused ion beam etching and characterised using Fourier spectroscopy and the field distributions on the gratings have been studied using Finite Difference Time Domain modelling. Realistic grating structures have been modelled based on focused ion beam cross sections and these results are in good agreement between measured and modelled results. The roles of surface plasmon polaritons and slot modes are highlighted in the strong broadband absorbance that can be achieved with these structures.

Keywords: Absorption, Thermal, Nickel, Plasmonics, Solar, Energy

1. INTRODUCTION

Over a century ago, narrowband absorption of light by diffraction gratings became known as “Wood’s anomalies” after their discoverer, R W Wood [1]. Since the realisation that these anomalies were due to localised surface waves [2] and eventually photon-induced plasma excitations [3] the field of plasmonics emerged. This has found application in many areas of photonics including radiation guiding, light trapping, sensing and surface enhanced Raman scattering [4] as well as guiding light below the diffraction limit [5]. Another important application of plasmonics is the absorption of light [6]. Due to the strong, localised fields that occur in plasmonic nanostructures and metamaterials [4], strong absorption of incident electromagnetic radiation can be achieved when working with plasmonic materials [7]–[9].

Solar thermal energy converters are an important renewable energy technology[10] and it is critical that they absorb as much of the incident solar electromagnetic spectrum as possible whilst minimising radiation losses [10]. Key parameters in coatings for solar thermal energy converters are spectral absorptivity and emissivity where absorptivity is defined by how much incident solar radiation is absorbed by a surface and emissivity is the total amount of radiation re-emitted by the structure compared to a perfect blackbody [10]. The ideal spectral profile of a solar thermal absorber would be zero reflectance for $0.3 \leq \lambda \leq 3$ μm and unity reflectance for $3 \leq \lambda \leq 100$ μm [11]. Ideally, this spectral response should be maintained across a wide range of incidence and emission angles and a surface with these spectral properties would then have minimum energy wasted as re-radiated heat. Excitation of surface plasmon polaritons (SPPs) on a metal surface allows us to create localised field resonances with light bound to a metal-air interface. These effects can make even very reflective surfaces perfect absorbers at desired wavelengths [12]. It has been shown that by fabricating sub-wavelength, deep (≥100nm) periodic arrays of grooves in plasmonic materials, SPPs can be excited even in the zero-order region of the spectrum, where diffraction does not occur and the grating would be expected to act as a mirror [13, 14]. This occurs because strong absorption occurs via coupled modes in the slots [14] also known as gap surface plasmon polaritons (GSPPs). The strong resonant absorption can then be controlled using the photonic modes supported by the structure by altering the shape (width and depth) of the grooves and the separation between grooves [15]. In the case of a solar absorber, this can allow us to tailor the surface to position these resonances at frequencies within the solar region of the spectrum whilst utilising a metal’s natural reflective properties in the infrared to minimise surface emission. Surfaces that are designed with these effects are known as plasmonic black-metal absorbers due to their black appearance in the visible [16]. Recently sub-wavelength nickel and palladium gratings have been studied [16] and it was found that linear and 2D grating structures dramatically increased optical absorptance at normal incidence. This paper investigates similar gratings, using both measurements and FDTD modelling. However, here, the grating pitch is much closer to the wavelength of incident light leading to potentially different regimes of operation and we also demonstrate how angle of incidence effects the absorptance response. The grating pitch regime is also of interest in respect to mass-fabrication techniques such as Displacement Talbot Lithography [17] where structures on the order of half a micron may be much more feasible for mass fabrication. The use of nickel is important for solar

thermal absorbers since the working temperature can be very high (>800 deg C) and the high melting point of nickel (1,455 °C) and relatively low cost makes it ideal for such high temperature applications.

We have previously performed extensive FDTD modelling of such structures [19] and this paper presents fabrication, measurement and further in-depth modelling of the structures. Section 2.1 describes the focused ion-beam (FIB) milling process used to create the samples and shows cross sections of fabricated structures. Section 2.2 shows measured results using Fourier spectroscopy [18]. Section 3 shows Finite Difference Time Domain modelling results, which are used to further the understanding of the optical behaviour.

2. RESULTS

2.1 Fabrication

Samples were fabricated by first sputtering nickel onto a glass substrate then using FIB to etch 20x20µm groove arrays with varying depths. A FEI FIB200 series FIB was used to etch the 200nm nickel films using a stream file to dictate the etch pattern. The etch was performed at a magnification of 20K and a beam current of 70pA. The number of repetitions for etch pattern was incremented sequentially from 4-7 to vary the depth of the grating structures. The four gratings had nominal periods, *p* of 515nm and aspect ratio of 0.8 with varying depth profiles. Figure 2 show optical microscopy images of the four nanostructures.

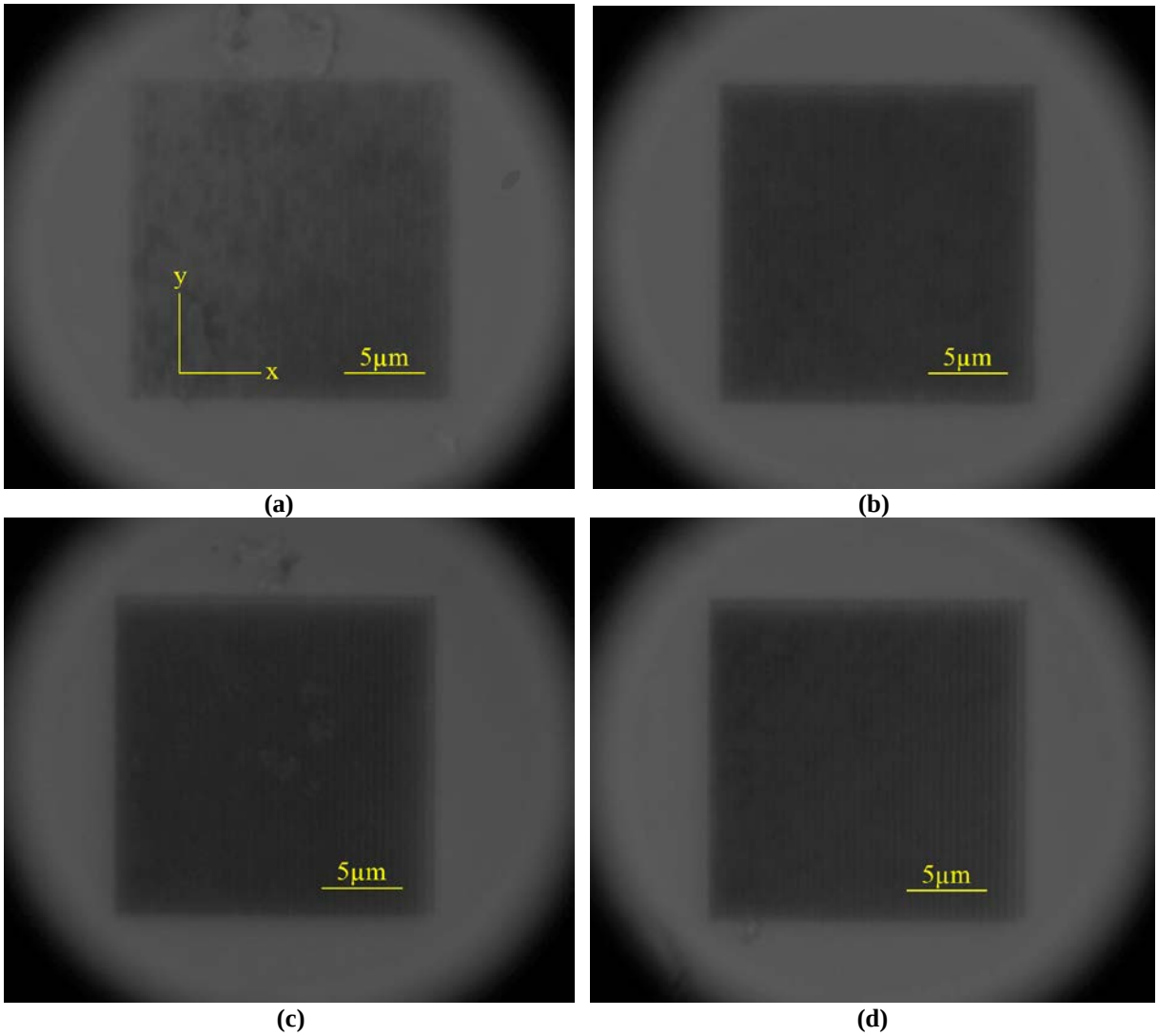

(a) **(b)**

(c) **(d)**

*Figure 1. Optical microscopy of grating structures illuminated with E_x-polarised light fabricated using ion-beam milling. The grating grooves are orientated parallel to the y-axis (**a**) Grating 1 (4 repetitions), (**b**) Grating 2(5 repetitions), (**c**) Grating 3(6 repetitions), (**d**) Grating 4(7 repetitions)*

The images in figure 1 were illuminated using an optical light source with a spectral range of 300-2500nm but limitations of the optical path and the CMOS camera mean that the images only account for the 400-950nm range. The brightness of the grating area decreases with the first three gratings when illuminated with E_x-polarised light, achieved by use of a polariser in the illumination path. This indicates increased optical absorption in the solar region and tending towards a black metal [19].

The gratings geometry is shown in figure 2, with nickel layer thickness, *t*, grating depth, *d*, period, *p* and aspect ratio, $a_r = a/p$.

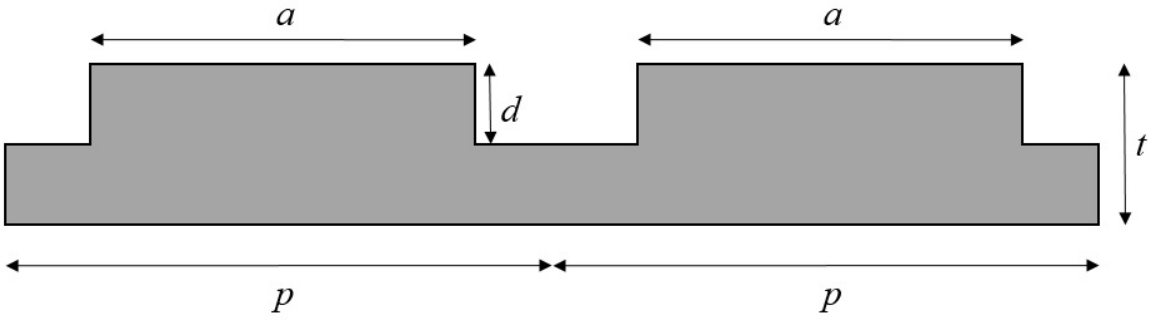

Figure 2. Diagram of grating geometry

Figure 3 shows FIB cross sections of the nanostructured 1D groove arrays after platinum deposition, used as part of the cross-sectioning process. The platinum layer deposition is applied to a very small imaged section of the grating and applied to create a contrast difference to be able to clearly see the nickel grating geometries. Below the platinum layer one can see the profile of the nanostructured nickel. Figure 3(a) shows Grating 1 produced with 4 beam passes. It can be seen that the grooves are just becoming visible and are measured to be on average 62nm deep. It also shows the measurements taken to form the average of each parameter of the grating. This has also been applied to the proceeding figures but has not been shown to reduce the cluttering of the images. Figure 3(b) shows Grating 2 and here the groove array is clearly defined and the uniformity of the structure has improved but there is still variation between the grooves. The depth is averaged to be 100nm, along with the period at 515nm and the aspect ratio is 0.8. There still remains a nickel layer at the base of the grooves.

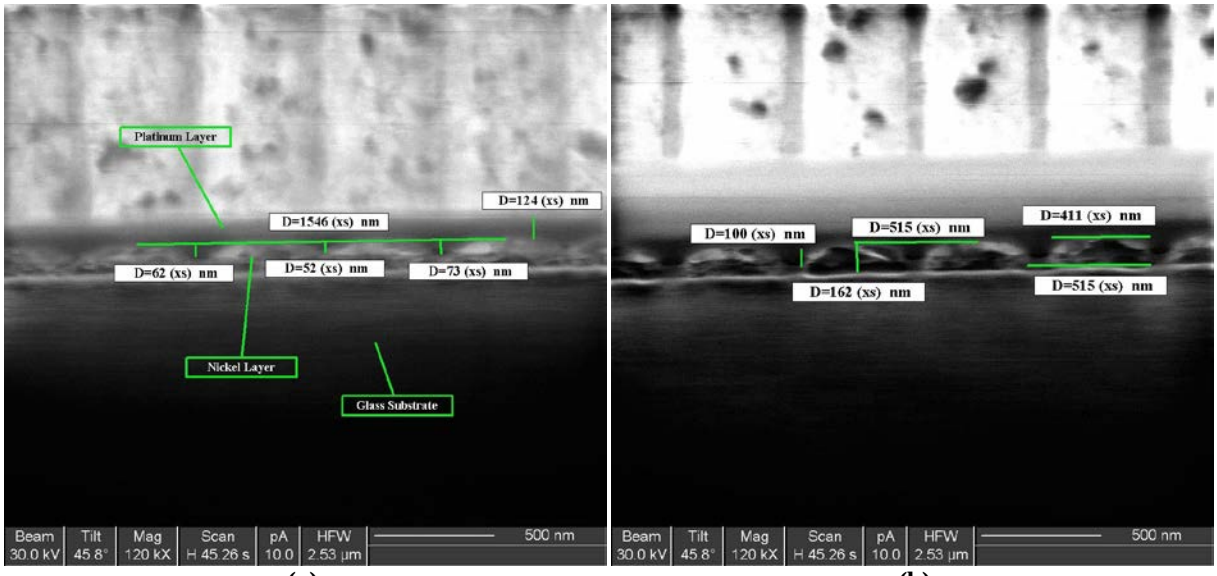

(a) **(b)**

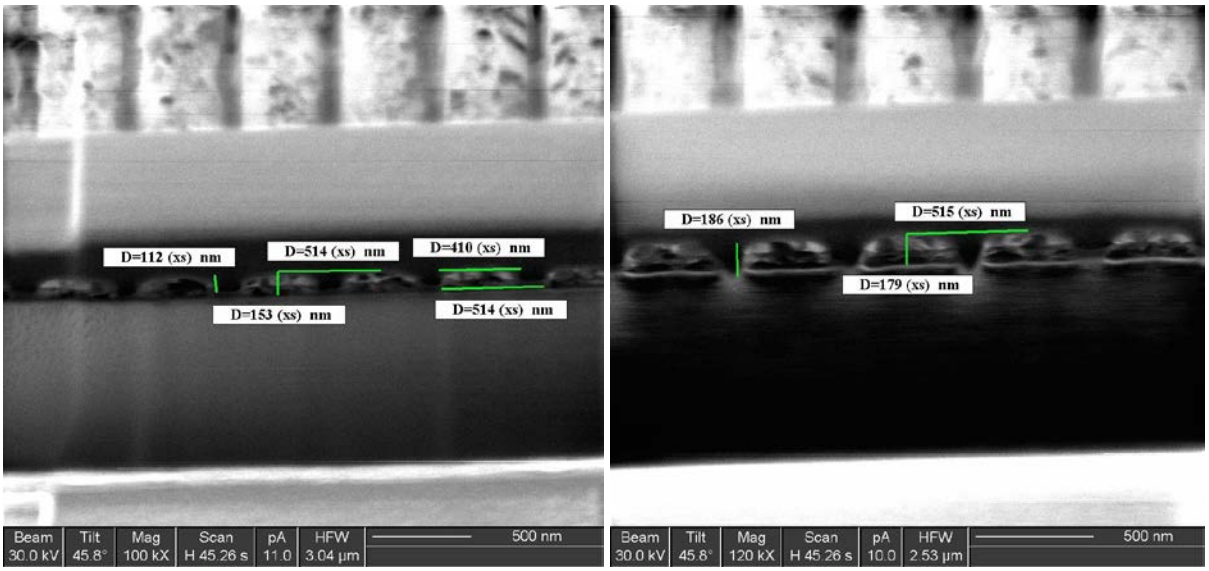

(c) **(d)**

*Figure 3. Focused ion beam cross-sections of nickel gratings using platinum deposition. (**a**) Grating 1, (**b**) Grating 2, (**c**) Grating 3, (**d**) Grating 4*

Figure 3(c) shows grating 3 has a depth profile that is almost as deep as the thickness of the nickel, with a much thinner layer of nickel below the nanostructure. This is interesting as it has been demonstrated in FDTD simulation that a thin lower layer of nickel can broaden the absorbance response of the structure in the optical regime [20]. Higher contrast images reveal that the thickness of nickel remaining in the grating channels of grating 3 is 41nm (images not included). For a layer of nickel of this thickness the transmittance is negligible with a maximum of 0.035 across this wavelength range. Grating 4, as shown in figure 3(d), has 7 passes of the focused ion beam with the nickel layer being etched through completely and in some grooves the glass substrate has been etched as well. Table 1 summarises the geometry of the fabricated gratings.

Grating No.	Thickness	Period	Depth	Aspect Ratio	Pt Layer
1	176nm ± 7.5nm	515nm	62nm ± 9.2nm	0.8	124nm
2	162nm ± 8nm	515nm	100nm ± 4nm	0.8	401nm
3	153nm ± 8.2nm	514nm	112nm ± 5.7nm	0.8	754nm
4	179nm ± 7.5nm	515nm	186nm ± 6.9nm	0.8	649nm

Table 1: Measured nickel grating parameters determined by FIB cross-section

2.2 Optical Characterisation

Each grating structure has been optically characterised in the 450nm-950nm spectral range using Fourier microscopy to obtain reflectance over a wide angular range (-54° to +54°). This imaging technique performs a spatial Fourier transform of the reflectance at each incident angle of a Kohler illuminated sample, which provides extremely even illumination. We can then spatially measure the reflectance at each angle by imaging the back focal plane (BFP) of the sample objective and collecting light along the plane of the image using a spectrometer [18]. For an interface, it can be assumed that incident light can be only reflected (R), transmitted (T) or absorbed (A) and therefore we can make the relation that $R+T+A=1$. Using this relation and creating structures where transmitted power, $T=0$, we can then calculate the absorptance using the relation $A=1-R$.

Figure 4 shows the measured absorptance, calculated using the relation stated above, or the measured reflectance if there is the possibility of non-negligible transmission in the sample. The thickness of the nanopatterned nickel layer means that transmitted power in the first three cases can be assumed to be zero and we can calculate the absorptance using the measured reflectance data. Figure 4 shows the response of gratings 1-4 under illumination by E_x-polarised light i.e. that light is polarised perpendicular to the grating grooves such that diffraction and plasmonic effects can occur. When looking at figure 4(a)

the centre of the *x*-axis (normal incidence), we see a distinct absorptive peak at around 600 nm that diminishes at longer wavelengths. This occurs due to the excitation of SPPs due to the additional momentum provided by the grating which results in phase matching between the incident field and the SPP. This peak in absorptance then shifts to longer wavelengths as the incident angle increases as described by the phase matching condition [4].

Figure 4(b) shows the measured absorptance of Grating 2, with the absorptance being larger than Grating 1 and having a wider bandwidth. The depth of the grating has increased to 100nm and the total thickness of the grating has reduced further to 162nm due to a longer etch time in the FIB. It is worth noting that the bandwidth of the resonant absorption has increased significantly with respect to grating 1, suggesting the coupling to the SPPs is now stronger.

As we increase the depth of the grating further and look at the response of Grating 3 in figure 4(c) we can see that the bandwidth of the enhanced absorption response has again increased. With an extra beam pass, the depth of the grating has increased further to 133nm and the total thickness of the grating has reduced to 153nm. In this case, we obtain the widest bandwidth of absorptance and thus we believe this is the optimum grating depth for coupling to SPPs.

Grating 4 as shown in figure 3(d) has an etch depth deeper than the total thickness of the grating, where the ion beam has etched though the nickel layer and into the glass substrate. As this means transmission will be non-negligible, the relation A=1-R is not valid. Instead, we have looked at the reflectance data for the sample. figure 4(d) shows the measured reflectance of grating 4, we still see a very low reflectance with a minimum at around 700nm at normal incidence which again moves to longer wavelengths as angle of incidence increases.

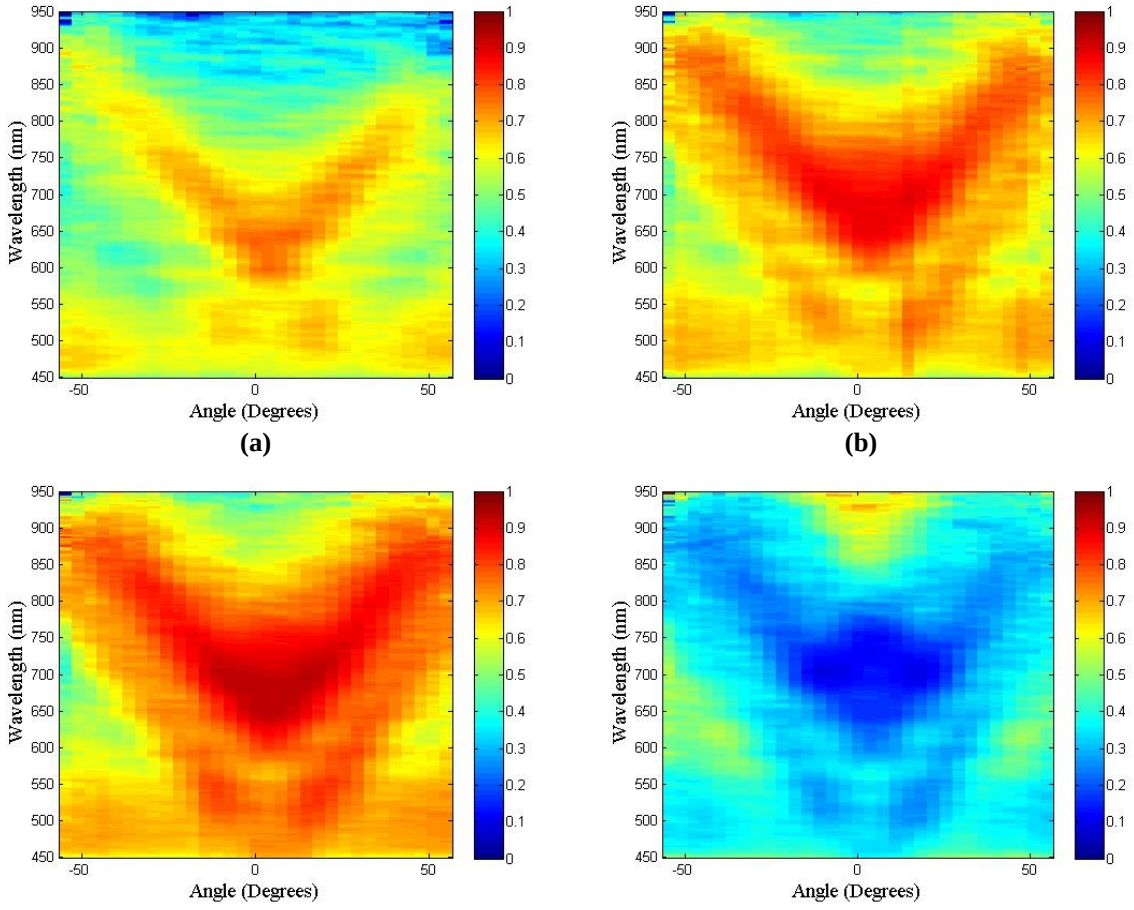

*Figure 4. Measured absorptance or reflectance of gratings 1-4 illuminated with E_x-polarised light from 450nm-950nm over -54°-54° angular range. (**a**) Grating 1, Absorptance, (**b**) Grating 2, Absorptance, (**c**) Grating 3, Absorptance, (**d**) Grating 4, Reflectance*

Figure 5 shows the measured absorptance or reflectance of gratings 1-4 at normal incidence along with that of bulk nickel as a reference. When looking at the figure, we can clearly see the trend of increased

absorptance of the grating as the grating depth increases. Grating 1 has a peak absorptance around 600-650nm which increases to 650-700nm as the grating depth increases as in the case of gratings 2-4. Finite Difference Time Domain modelling will now be used to investigate the trends observed in these experimental results.

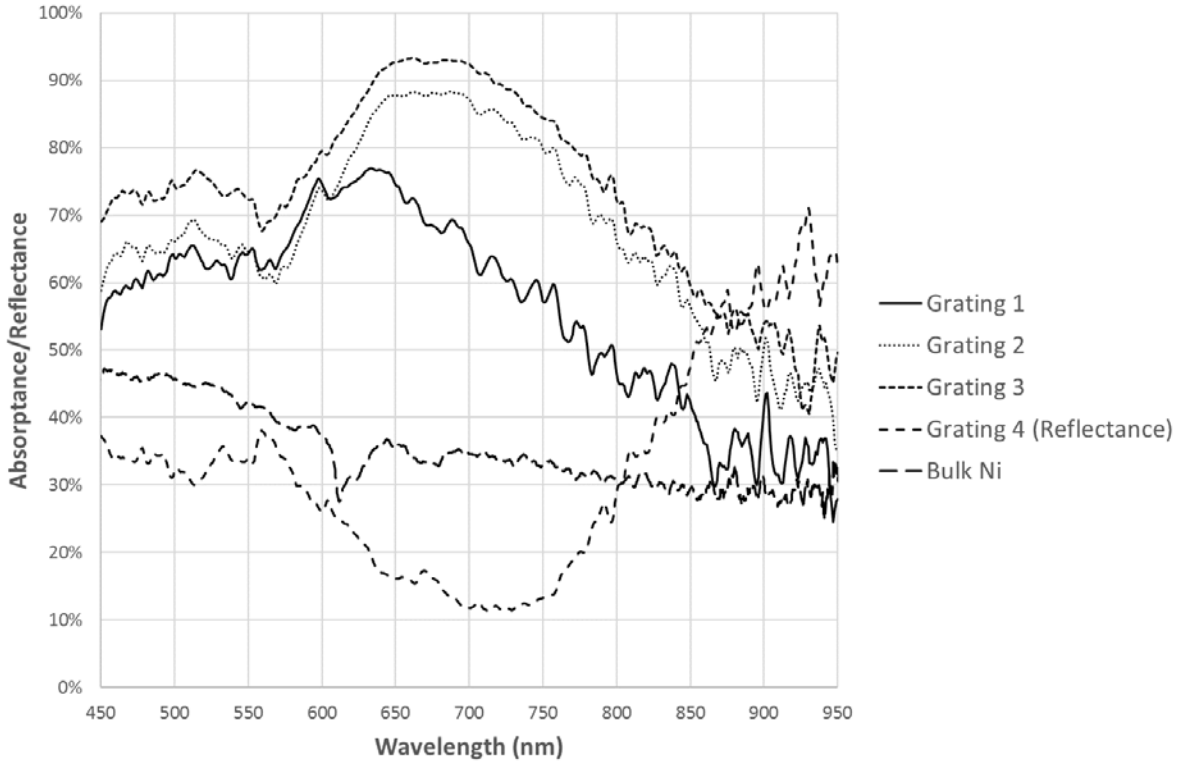

Figure 5. Measured absorptance or reflectance of Gratings 1-4 and bulk nickel illuminated with E_x-polarised light from 450nm-950nm at normal incidence

3. MODELLING

A FDTD model was developed to reproduce angular reflectance results as discussed above. The optical response of 1D linear grating structures were modelled using a commercial simulator [21]. The total transmitted, reflected and absorbed power was calculated over the 450nm-950nm wavelength range at a wide range of incident angles. The angular response was calculated by modelling illumination with a Gaussian beam and calculating reflected and transmitted power in the far-field. As can be seen from Figure 3, the grating structures do not have sharp corners when looking at their respective cross-sections, and this has been included in the FDTD model. Figure 6 shows unit cells of the grating structures that were modelled with figure 6(a) showing a unit cell geometry without rounded corners and figure 6(b) showing a unit cell using ellipses to form rounded corners for the grating structure. The rounded corners are made using ellipses with radii of 1/6 of the grating period and the depth of the grating.

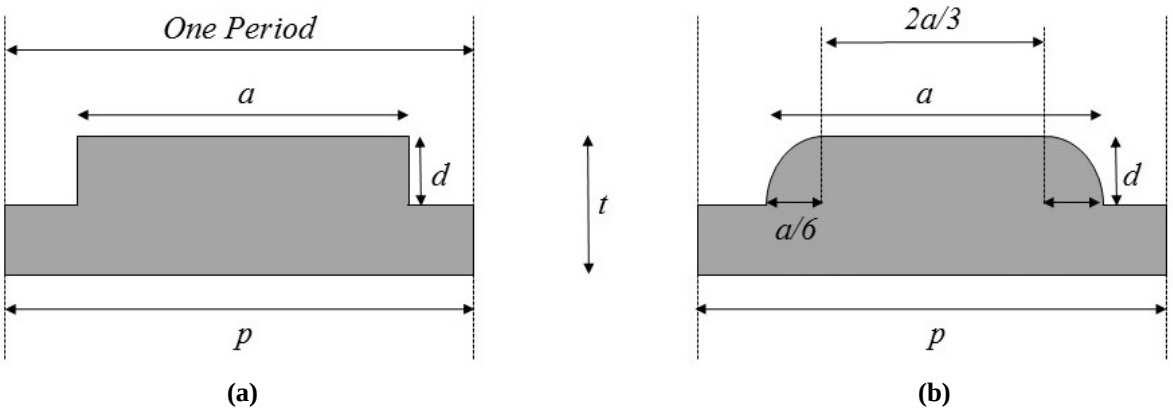

*Figure 6. Single periods of the grating structures implemented in the FDTD model, **(a)** without rounded corners **(b)** with rounded corners*

In the FDTD model we calculate the far-field transmitted and reflected powers with Gaussian illumination and include a simulated numerical aperture of 0.85, matching that used in the Fourier microscopy setup. As we are using a Gaussian illumination in the simulation, we are unable to use periodic boundary conditions as this would repeat the source. As a result, we have to use a finite-sized simulation with Perfectly Matched Layers at the boundaries and in our case we have simulated 40 periods which matches the number of periods that have been fabricated. Final simulation results are achieved by first simulating the near-field response of the structure and using a near-to-far transform to obtain the far-field response. By doing so we can see the angular distribution of the fields at each wavelength using only a single FDTD simulation run, saving computational time whilst also getting more accurate simulated results. The reflected and transmitted powers are also normalised using flat silver as a reference as used experimentally. This is achieved by running two independent simulations and normalising the results from the main simulation run to that of the flat bulk silver.

Figure 7 shows the simulated reflectance with and without rounded corners compared to the measured absorptance responses for grating 2, (period, p=515nm, thickness, t =162nm and depth, d = 100nm) as shown in figure 3(b). A dramatic shift of the peak absorptance wavelength towards that of the experimental result is observed. This highlights the importance of slot geometry in these gratings. This has been studied analytically in a number of cases [13, 15], but here we show results for a very realistic geometry that would be difficult to study analytically.

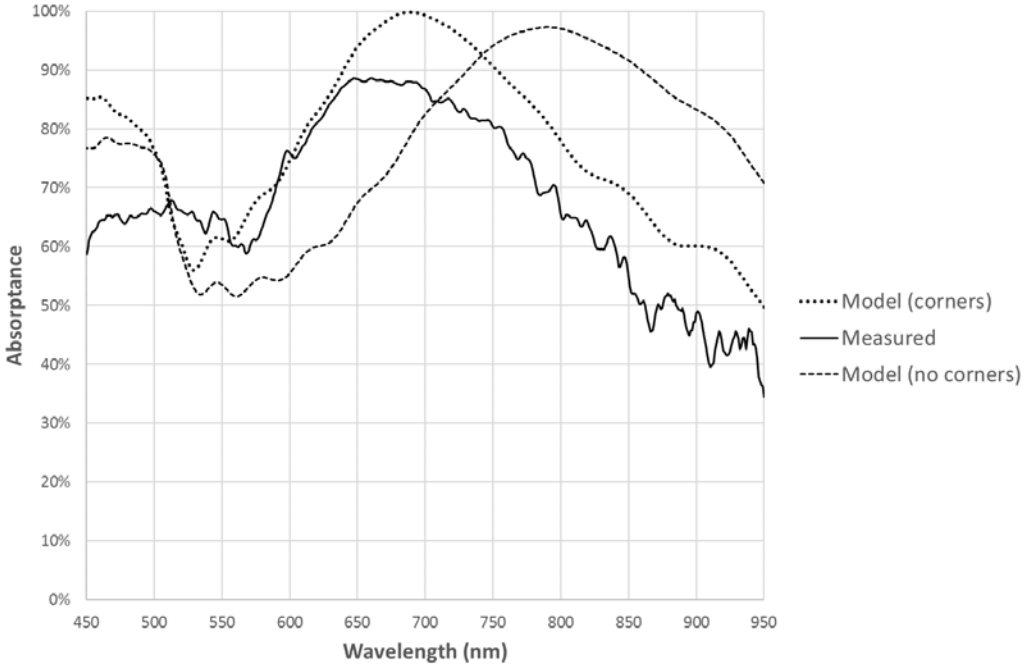

Figure 7. Modelled (with and without corners) and experimentally obtained absorptance of Grating 2

Figure 8(a) shows the modelled far-field absorptance response of the Grating 1, the result follows the trend of the measured optical absorptance with a peak around 600nm and the peak shifting to longer wavelengths as angle of incidence increases due to diffraction. As the grating depth increases with grating 2, figure 8(b) shows an increase in total absorption as well as the main band of absorption separating from the diffraction order. Comparing this with the measured response in figure 4(b), we see that this is in good agreement.

In figure 8(c) the model predicts a shift in peak absorptance to ~740nm however whilst the measured result in 4(c) shows an increase in absorptance, the peak remains in the same place. This could be due to the inhomogeneity of the sample as a result of FIB lithography. Factors such as beam drift and the homogeneity of the initial sample could be responsible for the disparity. The profile of the groove corners also dictates the position of the peak absorptance (as discussed in Section 3) and these have not been modelled exactly for each grating, with an approximation being used for all four gratings.

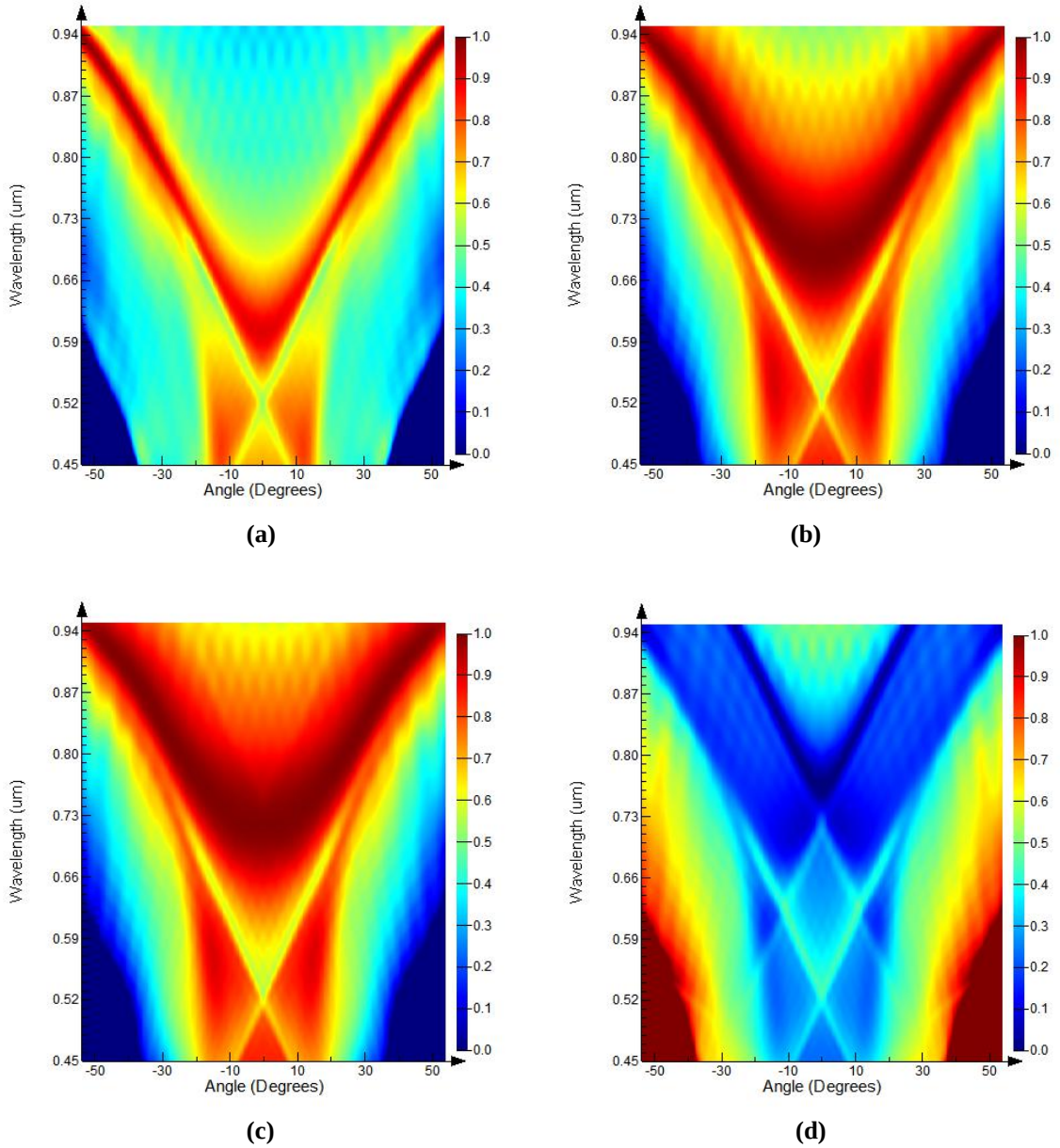

*Figure 8. Modelled absorptance or reflectance of gratings 1-4 illuminated with E_x-polarised light from 450nm-950nm over -54°-54° angular range. (**a**) Absorptance, (**b**) Absorptance, (**c**) Absorptance, (**d**) Reflectance*

Figure 8(d) shows results for grating 4 where the nickel film is now etched completely through. The modelled response of grating 4 in figure 8(d) shows a resonance at around 750nm at normal incidence

and is more clearly displayed in figure 9. The measured minimum reflectance shown in figures 4(d) is slightly offset when compared to figure 8(d). This could be again due to differences in the modelled grating geometry as now the model has to account for the shape of the etch into the glass as well as the nickel which in this case has been approximated to an ellipse. Again, we look at the normal incidence absorptance/reflectance in figure 9 below. We can again see the general trend of absorptance increasing as grating depth increases.

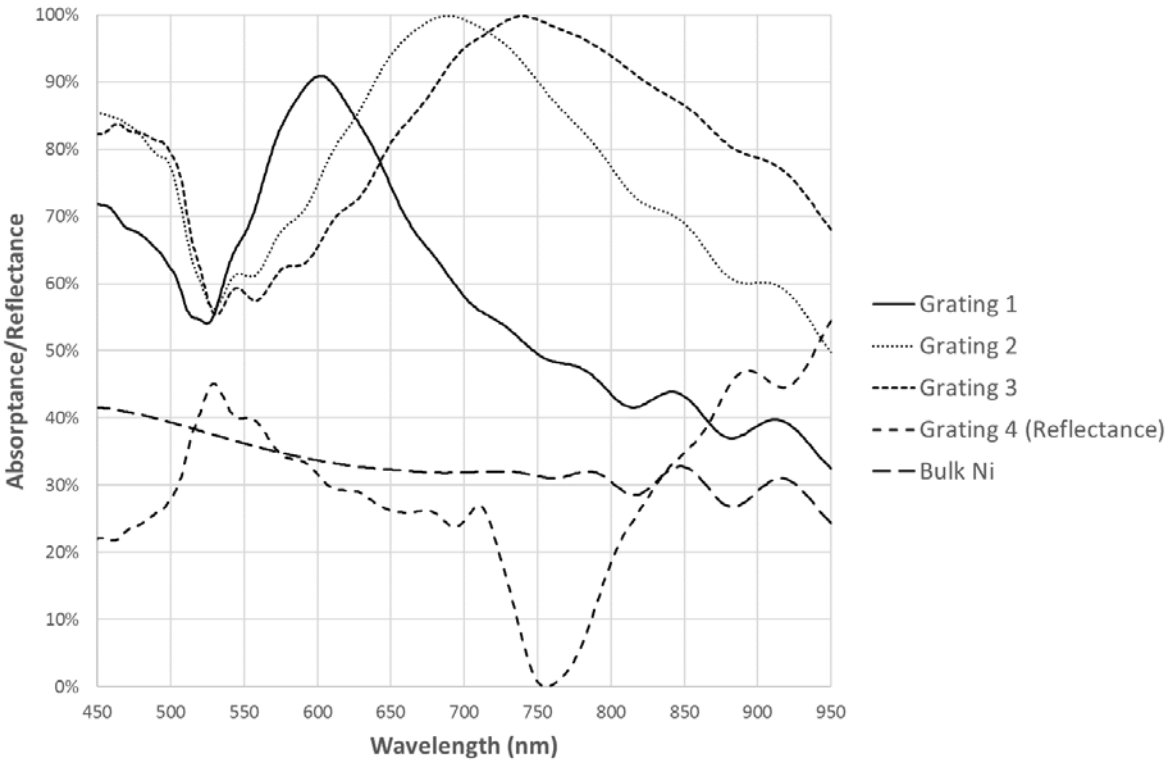

Figure 9. Modelled absorptance or reflectance of Gratings 1-4 and bulk nickel illuminated with E_x-polarised light from 450nm-950nm at normal incidence

By modelling in FDTD we can also look at the fields of the structure at particular wavelengths, we can then use these to look for highly localised electric fields that occur when SPPs are propagating and look at the magnetic field distribution at resonant wavelengths. For the following field snapshots, we are illuminating with a plane wave to observe the normal-incidence response of the grating structures.

The modelled electric field distributions under normal incidence plane wave illumination of gratings 1 and 3 at their respective resonant wavelengths (as can be seen by the peaks in figure 9) are shown in figure 10.

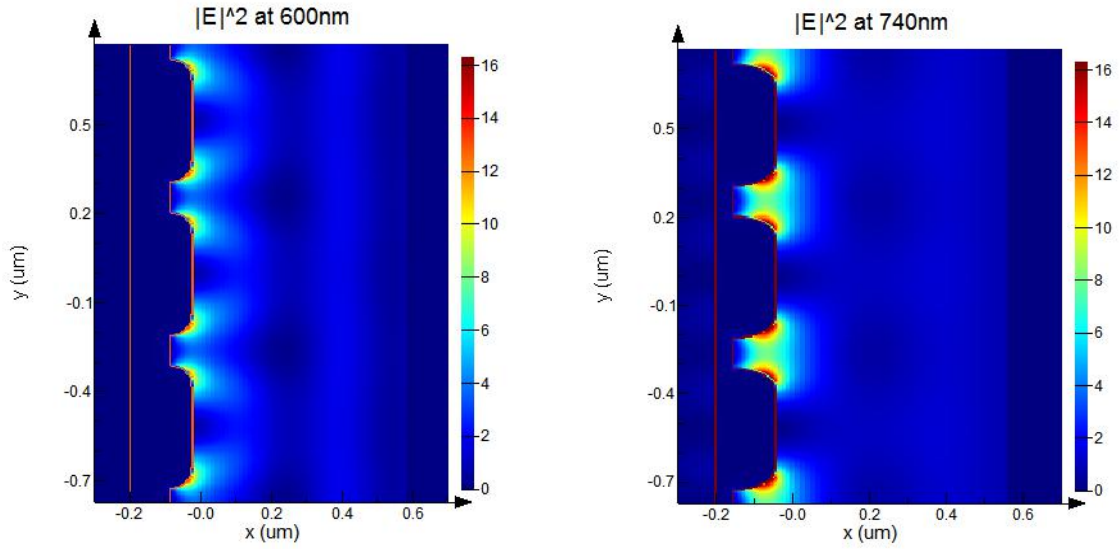

(a) **(b)**

*Figure 10. Modelled electric field distributions for gratings 1-3 at on-resonance wavelengths (**a**) Grating 1, (**b**) Grating 3*

When looking at the fields in figure 10 we can see strong localised electric field intensity at the corners of the grooves. Comparing figure 10(a) with 10(b) we can see as grating depth increases the strong, localised electric fields move down the grooves and have stronger coupling to one another whilst being more confined. As this occurs at the interface between a negative and a positive real dielectric constant material (nickel and air) this indicates supported surface plasmon polaritons. This resonant intensity enhancement at the corners of the grating combined with the strongly attenuating properties of the nickel leads to a strong absorption response by the material at these wavelengths. In figure 11 we look at the magnetic fields of gratings 1 and 3 at normal incidence.

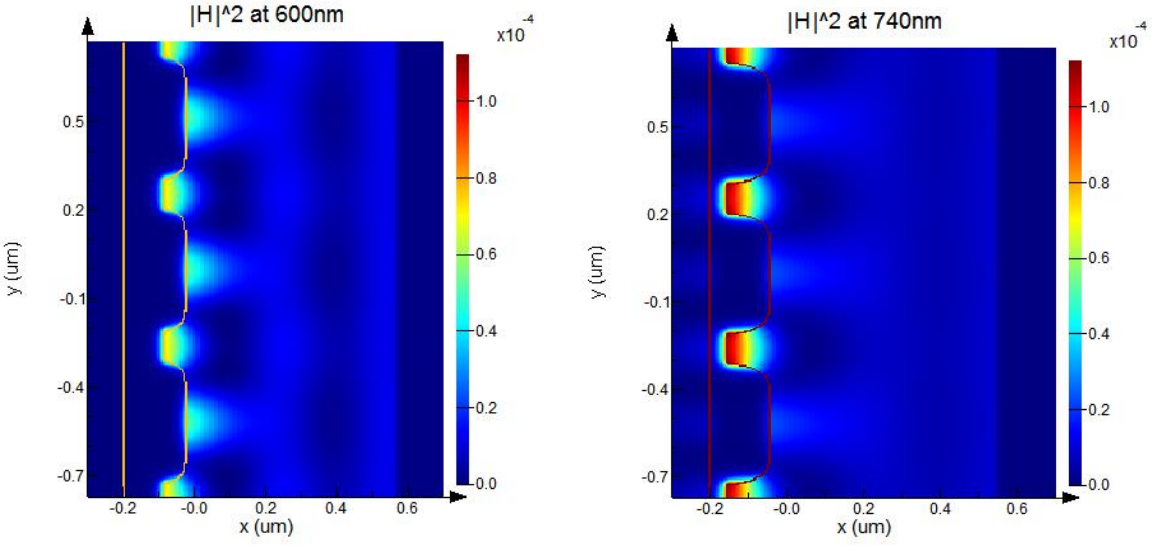

(a) **(b)**

*Figure 11. Modelled magnetic field distributions for gratings 1-3 at on-resonance wavelengths (**a**) Grating 1, (**b**) Grating 3*

The field snapshot in figure 11(a) shows the magnetic field intensity of grating 1. We can see the magnetic field intensity is concentrated within the grooves and as the incident wavelength is within the first diffraction order of the grating we also see the magnetic field supported along the top of the grating. This allows the slot modes that exist within the grooves to couple to one another leading to a supported resonant surface wave. As depth increases and we look at figure 11(b), the peak of the absorptance

moves to longer wavelengths and further away from the diffracted order. The resulting magnetic field supported along the surface of the grating then gets weaker, however as the depth of the grooves has increased, the supported slot modes dominate the absorption response at longer wavelengths. This leads to an absorption peak at longer wavelengths and a more broadband response as shown in figure 9.

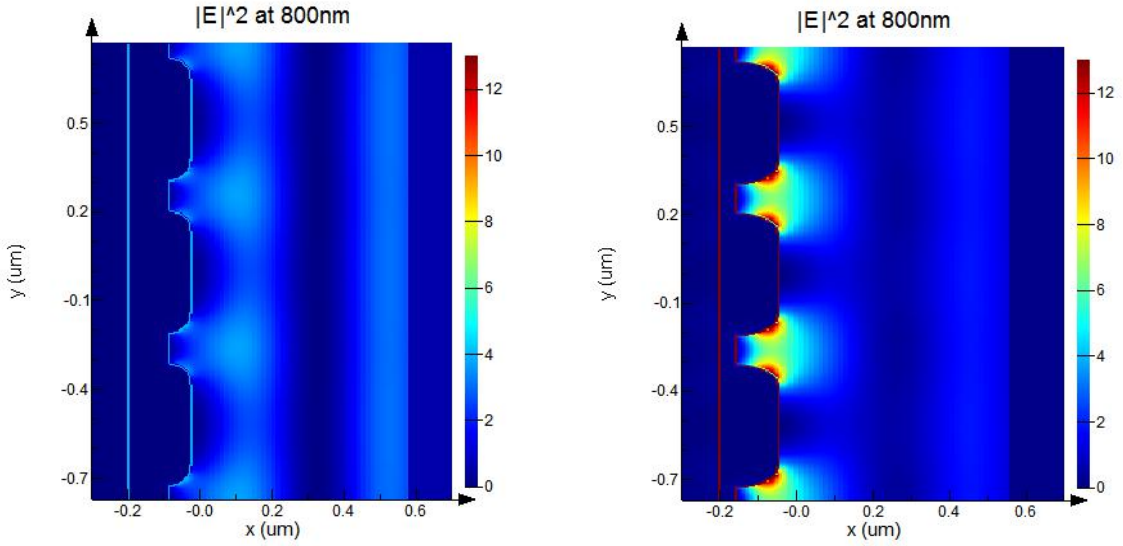

(a) **(b)**

*Figure 12. FDTD Modelled electric field distributions for gratings 1-3 at 800nm wavelength **(a)** Grating 1, **(b)** Grating 3*

In figure 12 we now look at the fields at 800nm which is a non-resonant wavelength for grating 1 but much closer to resonance in grating 3. In figure 12(a) we see the electric field at 800nm for grating 1 where the electric field intensity is far lower than at the resonant wavelength. As there is a significant amount of reflectance at this wavelength, we can see the field in the grooves matching the intensity of the incident and a resulting interference pattern. In figure 12(b) we can see strong localised field intensities at the corners of the grooves, however they are beginning to leak out further into free space if compared with figure 10(b). The absorptance of grating 3 remains high compared to bulk nickel at the 800nm wavelength as shown in figure 9. This indicates that the supported slot modes are still dominating the absorptance response at this wavelength.

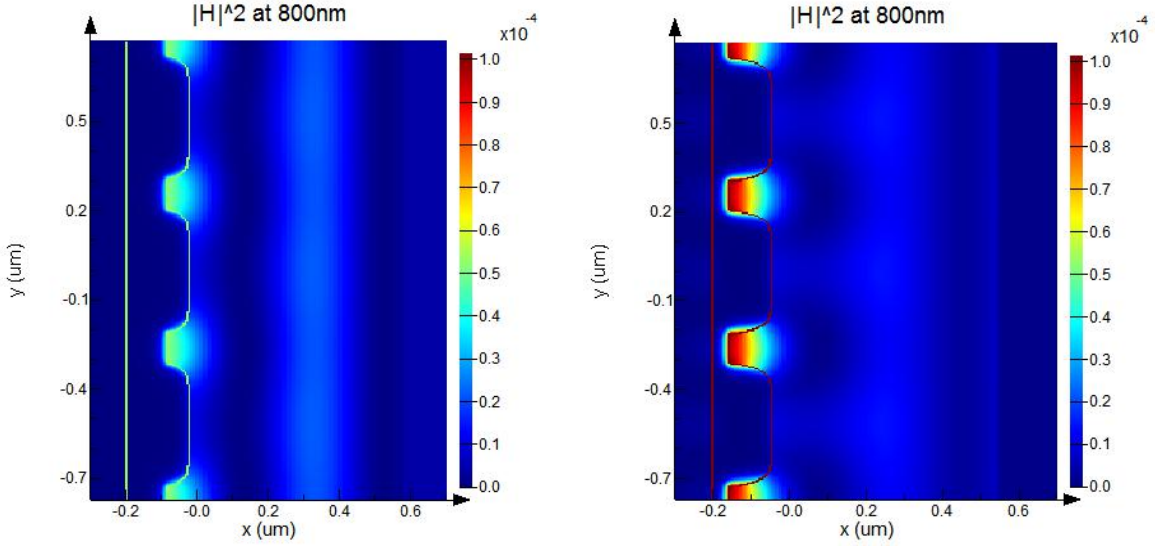

(a) **(b)**

*Figure 13. Modelled magnetic field distributions for gratings 1-3 at 800nm wavelength **(a)** Grating 1, **(b)** Grating 3*

Figure 13(a) shows the magnetic field response of grating 1 at 800nm. Here, we are at a far higher wavelength than the diffracted order and so we do not see a supported magnetic field along the surface of the grating. Both snapshots show that the magnetic field intensity is localised within the grooves. In figure 13(b) the magnetic field is almost totally confined within the groove whereas in figure 13(a) it is not as confined. Looking at figure 9, grating 3 is still more absorptive than bulk nickel at this wavelength indicating that the supported slot modes are leading to a dramatic increase in absorption. The broadband nature of this effect makes it ideal for absorbing a large portion of incident solar energy and a good candidate for solar thermal applications.

4. CONCLUSIONS

This paper has shown measured and modelled results for FIB patterned nickel gratings. These show that a dramatic increase in the optical absorptance can be obtained with careful choice of etch depth and period. By using a simple 1D linear grating structure, one can utilise plasmonic and diffractive effects to tailor the absorption response of a surface. Both the angular and wavelength dependence of the absorption have been investigated. We have used FDTD results to explore the coupling of supported modes within the grating grooves to surface waves which plays an important role in the operation of these structures. These results show that nanopatterned nickel gratings have potential for use in solar thermal energy converters where high temperature operation and low cost are required.

5. REFERENCES

[1] R. Wood, “On a remarkable case of uneven distribution of light in a diffraction grating spectrum,” *Proc. Phys. Soc. London*, vol. 18, no. 1, pp. 269–275, 1902.

[2] U. Fano, “The theory of anomalous diffraction gratings and of quasi-stationary waves on metallic surfaces (Sommerfeld’s waves),” *JOSA*, vol. 31, 1941.

[3] A. Otto, “Theory of Plasmon Excitation in Thin Films by Electrons of Non-Normal Incidence,” *Phys. status solidi*, vol. 22, no. 2, pp. 401–406, 1967.

[4] S. A. Maier, *Plasmonics: Fundamentals and Applications*. Springer US, 2010.

[5] D. K. Gramotnev and S. I. Bozhevolnyi, “Plasmonics beyond the diffraction limit,” *Nat. Photonics*, vol. 4, no. 2, pp. 83–91, 2010.

[6] L. C. Botten and I. T. Ritchie, “IMPROVEMENTS IN THE DESIGN OF SOLAR SELECTIVE THIN FILM ABSORBERS,” vol. 22, no. 3, pp. 421–426, 1977.

[7] M. C. Hutley and D. Maystre, “The total absorption of light by a diffraction grating,” *Opt. Commun.*, vol. 19, no. 3, pp. 431–436, 1976.

[8] N. I. Landy, S. Sajuyigbe, J. J. Mock, D. R. Smith, and W. J. Padilla, “Perfect Metamaterial Absorber,” *Phys. Rev. Lett.*, vol. 100, no. 20, p. 207402, 2008.

[9] C. Wu, B. Neuner, G. Shvets, J. John, A. Milder, B. Zollars, and S. Savoy, “Large-area wide-angle spectrally selective plasmonic absorber,” *Phys. Rev. B*, vol. 84, no. 7, p. 075102, 2011.

[10] S. A. Kalogirou, *Solar Energy Engineering Processes and Systems Second Edition*. 2014.

[11] C. Granqvist, “Spectrally selective coatings for energy efficiency and solar applications,” *Phys. Scr.*, vol. 32, pp. 401–407, 1985.

[12] J. Hao, L. Zhou, and M. Qiu, “Nearly total absorption of light and heat generation by plasmonic metamaterials,” *Phys. Rev. B*, vol. 83, no. 16, p. 165107, Apr. 2011.

[13] I. Hooper and J. Sambles, “Dispersion of surface plasmon polaritons on short-pitch metal gratings,” *Phys. Rev. B*, vol. 65, no. 16, p. 165432, Apr. 2002.

[14] M. Sobnack, W. Tan, N. Wanstall, T. Preist, and J. Sambles, “Stationary Surface Plasmons on a Zero-Order Metal Grating,” *Phys. Rev. Lett.*, vol. 80, no. 25, pp. 5667–5670, 1998.

[15] W.-C. Tan, T. Preist, J. Sambles, and N. Wanstall, “Flat surface-plasmon-polariton bands and resonant optical absorption on short-pitch metal gratings,” *Phys. Rev. B*, vol. 59, no. 19, pp. 12661–12666, 1999.

[16] J. Beermann, R. L. Eriksen, T. Søndergaard, T. Holmgaard, K. Pedersen, and S. I. Bozhevolnyi, “Plasmonic black metals by broadband light absorption in ultra-sharp convex grooves,” *New J. Phys.*, vol. 15, pp. 1–7, 2013.

[17] H. H. Solak, C. Dais, and F. Clube, “Displacement Talbot lithography: a new method for high-resolution patterning of large areas.,” *Opt. Express*, vol. 19, no. 11, pp. 10686–10691, 2011.

[18] M. L. Garcia, “Self Assembled Photonic-Plasmonic Crystals for Light control at the Nanoscale,” 2011.

[19] V. G. Kravets, F. Schedin, and A. N. Grigorenko, “Plasmonic blackbody: Almost complete absorption of light in nanostructured metallic coatings,” *Phys. Rev. B*, vol. 78, no. 20, p. 205405, 2008.

[20] N. Ahmad, J. Stokes, and M. J. Cryan, “Solar absorbers using 1D and 2D periodic nanostructured nickel films,” *J. Opt.*, vol. 16, no. 12, p. 125003, 2014.

[21] “Lumerical Solutions, Inc.” [Online]. Available: http://www.lumerical.com/tcad-products/fdtd/.